Journal of Solid State Chemistry 184 (2011) 523–530

Contents lists available at ScienceDirect

Journal of Solid State Chemistry

journal homepage: www.elsevier.com/locate/jssc

Valence and origin of metal–insulator transition in Mn doped $SrRuO_3$ studied by electrical transport, X-ray photoelectron spectroscopy and LSDA+U calculation

Ranjan K. Sahu [a,*], Sudhir K. Pandey [b], L.C. Pathak [a]

[a] Materials Science and Technology Division, National Metallurgical Laboratory, CSIR, Jamshedpur 831007, India
[b] UGC-DAE Consortium for Scientific Research, University Campus, Khandwa Road, Indore 452001, India

ARTICLE INFO

Article history:
Received 29 June 2010
Received in revised form
13 December 2010
Accepted 4 January 2011
Available online 8 January 2011

Keywords:
Metal–insulator transition
X-ray photoelectron spectroscopy
Valence study

ABSTRACT

We have studied the valence and electronic properties of Mn doped $SrRuO_3$ using electrical transport measurement, X-ray photoelectron spectroscopy (XPS) and local (spin) density approximation plus Coulomb interaction strength calculation (LSDA+U). The resistivity data revealed that the system undergoes transition from metal to insulator at the critical Mn doping level, $x \sim 0.2$, which is accompanied by the structural transition from orthorhombic to tetragonal crystal symmetry. Besides, the significant reduction of the spectral weight at the coherent zone (0.8 eV) of the valence band is observed for $x > 0.2$. The core XPS spectra suggest that both the transition elements exist in the mixed ionic pair, $Ru^{+4}/Ru^{+5} \leftrightarrow Mn^{+3}/Mn^{+4}$. The detail analysis of the results suggests that the Coulomb correlation effect in conjugation with localization of the charge carriers predominate over the mixed ionic pair effect and responsible for the metal–insulator transition in the series.

1. Introduction

$SrRuO_3$ has received a special attention in the recent years because of high chemical stability, good metallic and thermal conductivity, magnetic properties ($T_C \sim 165$ K), and easy epitaxial growth on various perovskite substrates. Owing to these properties, $SrRuO_3$ is an important candidate for normal metal layers in Josephson junctions, as an electrode in microelectronic devices, etc. [1,2]. Since different kinds of electron mediated phenomenon such as Coulomb and exchange interactions are controlled by foreign ions, efforts have been made by doping 3d transition elements at the Ru-site to further improve magnetic and electronic properties or to introduce new functional properties like spintronic in $SrRuO_3$ [3,4]. Among 3d elements, Mn and Ru combination in the crystal lattice of the perovskite compounds exhibit unique physical properties. Notably, Mn induced ferromagnetism in G-type of antiferromagnetic $CaRuO_3$ insulator, Ru acted as a charge ordering dilutor in $Nd_{0.5}Sr_{0.5}MnO_3$ manganite, mixed ionic pair between Ru and Mn formed in $La_{0.7}Sr_{0.3}Mn_{0.9}Ru_{0.1}O_3$, and Ru induced spin rotation in $La_{1.2}Sr_{1.8}Mn_2O_7$ layered manganite [5–9]. These properties are explained based on the existence of mixed valence states of Ru ions (Ru^{+4} and Ru^{+5}), and their participation in the double exchange ferromagnetic interaction with the mixed valence states of Mn, Mn^{+3}/Mn^{+4} since the e_g and t_{2g} parentage of Ru^{+5} is similar to the Mn^{+4} ion. Therefore, the combination of Ru and Mn in the perovskite manganite systems suggests that these two diagonally placed elements in the periodic table are efficient and unique pair for unusual magnetic and electronic properties. However, doping of Mn in the metallic $SrRuO_3$ drives the system into insulating state and the properties are same as observed in other 3d transition elements doped $SrRuO_3$ [10]. The experimental conductivity data of Mn doped $SrRuO_3$ samples exhibit a large deviation with respect to the conductivity behavior observed in Ru doped manganite samples [5–9]. The underlying conduction mechanism for such deviation is still unknown. This motivates us to study the valence and electronic properties of $SrRu_{1-x}Mn_xO_3$ to understand the associated mechanism related to the metal–insulator transition at the critical doping concentration, $x \sim 0.2$.

Recently, Kolesnik et al. [10] have reported the structural and magnetic phase diagram of the $SrRu_{1-x}Mn_xO_3$ series studied by neutron spectroscopic method. They observed that the magnetic structure of $SrRu_{1-x}Mn_xO_3$ is equivalent to the magnetic structure of electron doped manganite system, $Sr_{1-x}La_xMnO_3$. The different C and G-type of magnetic ordering in $SrRu_{1-x}Mn_xO_3$ is discussed based on the mixed Mn^{+4}/Mn^{+3} ions. This suggests that the formation of the mixed Mn valence can be induced in the system either by doping Ru at the Mn site or La at the Sr-site. However, no reports have been emphasized on the correlation parameters to understand the electronic properties of

* Corresponding author. Fax: +91 06572345213.
E-mail address: rksahu@nmlindia.org (R.K. Sahu).

0022-4596/$ - see front matter © 2011 Elsevier Inc. All rights reserved.
doi:10.1016/j.jssc.2011.01.005

$SrRu_{1-x}Mn_xO_3$. Photoemission spectroscopy is a direct technique to determine the valence states of an atom and powerful method to understand about the effect of various electronic interaction parameters on the conductivity of $SrRuO_3$. For instance, photoemission spectroscopic studies revealed that electron correlation between the *d* electrons is significant in $SrRuO_3$ in spite of the relatively extended 4*d* wave functions compared to the 3*d* wave functions in 3*d* transition-metal oxides [11]. The magnitude of the on-site Coulomb interaction *U* is also found to be sizable. Consequently, the observed spectral line shape of the Ru 4*d* band is spread over a wide energy range and the emission intensity at the Fermi level is weakened compared to the band-structure calculation. Besides, the core level spectra of Ru have been studied extensively to reveal the Mott transition phenomenon, where the satellite structure manifested the conduction mechanism of ruthenates [12]. Therefore, study of the valence band as well as core level spectra of Mn doped $SrRuO_3$ using photoemission spectroscopy in association with calculated density of states would give complete electronic structure of the system, which would be useful to explain the observed metal–insulator transition in $SrRu_{1-x}Mn_xO_3$.

In this article, we have firstly studied the resistivity properties of the polycrystalline $SrRu_{1-x}Mn_xO_3$ samples to derive the nature of doping effect on the conduction properties that shows Mn drives the system from itinerant metallic state to insulating state at the critical doping concentration, $x \sim 0.2$. Secondly, we have investigated valence band near the Fermi edge, and core Ru 3*d*, Ru 3*p*, Mn 2*p*, and Mn 3*s* peaks of $SrRu_{1-x}Mn_xO_3$ using photoemission spectroscopy to understand about the factors such as valence states of transition elements and effect of electron correlation parameters on the metal–insulator transition of the series. Thirdly, we have studied the valence band electronic structure using local (spin) density approximation plus Coulomb interaction strength (LSDA+*U*) calculation to support the experimental findings pertaining to the XPS results. The combination of experimental and theoretical data explains the origin of metal–insulator transition in $SrRu_{1-x}Mn_xO_3$.

2. Experimental and computational details

Samples were prepared by solid state reaction route followed by sintering in the form of pellets at 1200 °C for about 72 h with four times intermittent grinding to achieve large grain sizes and obtain phase purity samples. The purity of the samples was checked by the XRD technique (Bruker, D8 DISCOVER) using Co-*K*α as an X-ray source ($\lambda = 1.79$ Å). The transport properties were measured using four-point probe method. Photoelectron spectroscopy measurements at room temperature were carried out using SPECS spectrometer, GmbH, Berlin, Germany. The measurements were performed using Al-*K*α monochromator X-ray source ($h\nu = 1486.6$ eV). The base pressure of the chamber was 2.3×10^{-10} Torr and during data acquisition the pressure was $\sim 5 \times 10^{-9}$ Torr. The total resolution for XPS was ~0.6 eV at pass energy of 25 eV. Photoelectron measurements were performed on freshly fractured samples and the charging effect, if any, was checked using electron flood gun attached to the spectrometer. The deconvolution of the Ru peak was carried out using the following procedure; each peak was represented by symmetric function generated by a Lorentzian function convoluted with a Gaussian. The Lorentzian function represents the lifetime broadening effect while the Gaussian function supposes to account for all other broadening including resolution broadening. Besides, one function for Sr $3p_{1/2}$, two more doublets were used; one doublet for the main Ru 3*d* spin–orbit split peaks and the other for the weak satellite feature, with the intensity ratio between the spin–orbit split components being fixed at 1.5 which determined by the degeneracy ratio. The full width half maximum of all the peaks pertaining to Ru 3*d* peak was kept constant (1.9 eV).

The spin polarized electronic structure calculations of $SrRuO_3$ and $Sr_{0.75}Mn_{0.25}RuO_3$ compounds were carried out using LmtArt 6.61 [13]. For calculating charge density, full-potential linearized muffin-tin orbital method working in plane-wave representation was employed. In the calculations, we have used the muffin-tin radii of 3.119, 2.134, 1.61, and 1.615 a.u. for Sr, Ru (Mn), O1, and O2, respectively. The charge density and effective potential were expanded in spherical harmonics up to $l=6$ inside the sphere and in a Fourier series in the interstitial region. The initial basis set included 5*s*, 4*p*, and 4*d* valence, and 4*s* semicore orbitals of Sr; 5*s*, 5*p*, and 4*d* valence, and 4*p* semicore orbitals of Ru; 4*s*, 4*p*, and 3*d* valence, and 3*p* semicore orbitals of Mn; and 2*s* and 2*p* valance orbitals of O. The exchange-correlation functional of the density-functional theory was taken after Vosko et al. [14]. (6, 6, 6) divisions of the Brillouin zone along three directions for the tetrahedron integration were used to calculate the DOS. Self-consistency was achieved by demanding the convergence of the total energy to be smaller than 10^{-4} Ry/cell.

3. Results and discussion

Fig. 1 shows the temperature dependence of resistance for polycrystalline bulk $SrRu_{1-x}Mn_xO_3$ samples. The parent $SrRuO_3$ compound shows the metallic behavior (where $d\rho/dT > 0$) and a kink is observed close to the Curie temperature, $T_C \sim 165$ K. This kink has been attributed to the spin scattering of the carrier electron in the ferro-paramagnetic transition regime [15]. The similar resistivity behavior against temperature prevails in the system up to 10% of Mn doping. However, the temperature dependence resistance data for $x \geq 0.2$ show that the resistance increases (where $d\rho/dT < 0$) with decreasing temperature. It is observed that the resistance increased several folds for $x > 0.2$ at below $T = 50$ K. These results indicate that Mn doping drives the $SrRuO_3$ system from metallic state to insulating state at the critical doping, $x \sim 0.2$. The resistivity data and the critical doping concentration for the metal–insulator transition in polycrystalline Mn doped $SrRuO_3$ are consistent with the data reported earlier by Kolesnik et al. [10]. The metallic property of $SrRuO_3$ is explained based on the appearance of strong spectral weight near the Fermi

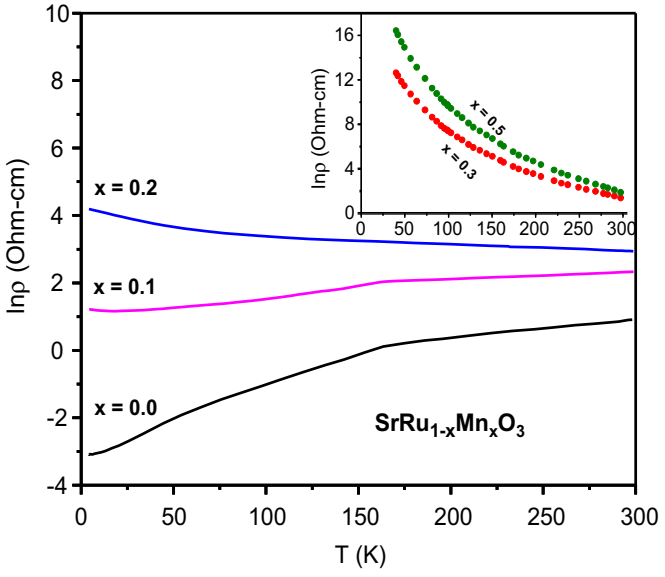

Fig. 1. Resistance as a function of temperature for $SrRu_{1-x}Mn_xO_3$.

level caused by strong hybridization between Ru 4*d* and O 2*p* orbitals, and itinerant character of 4*d* electrons. Substitution of Mn is expected to increase the spectral weight of $SrRuO_3$ by virtue of increasing charge carrier delocalization since Mn forms mixed ionic pair with Ru ($Mn^{+3}/Mn^{+4} \leftrightarrow Ru^{+4}/Ru^{+5}$) and the mixed pairs mediate double exchange ferromagnetic interaction as discussed earlier [5–9]. However, the resistivity of $SrRuO_3$ increases with Mn doping, which suggests a detail study is required to understand the role of doping ion on the electronic properties.

Extensive studies of the similar Mn based perovskite systems show that structural phase transition is also one of the factors responsible for the metal–insulator transition even though the mixed ionic pair (Mn^{+3}/Mn^{+4}) persists in the system [16–18]. Therefore, we have checked the phase transition structurally of these samples using XRD technique (Fig. 2) before we go for the detail analysis of the resistivity data. It is observed that the crystal

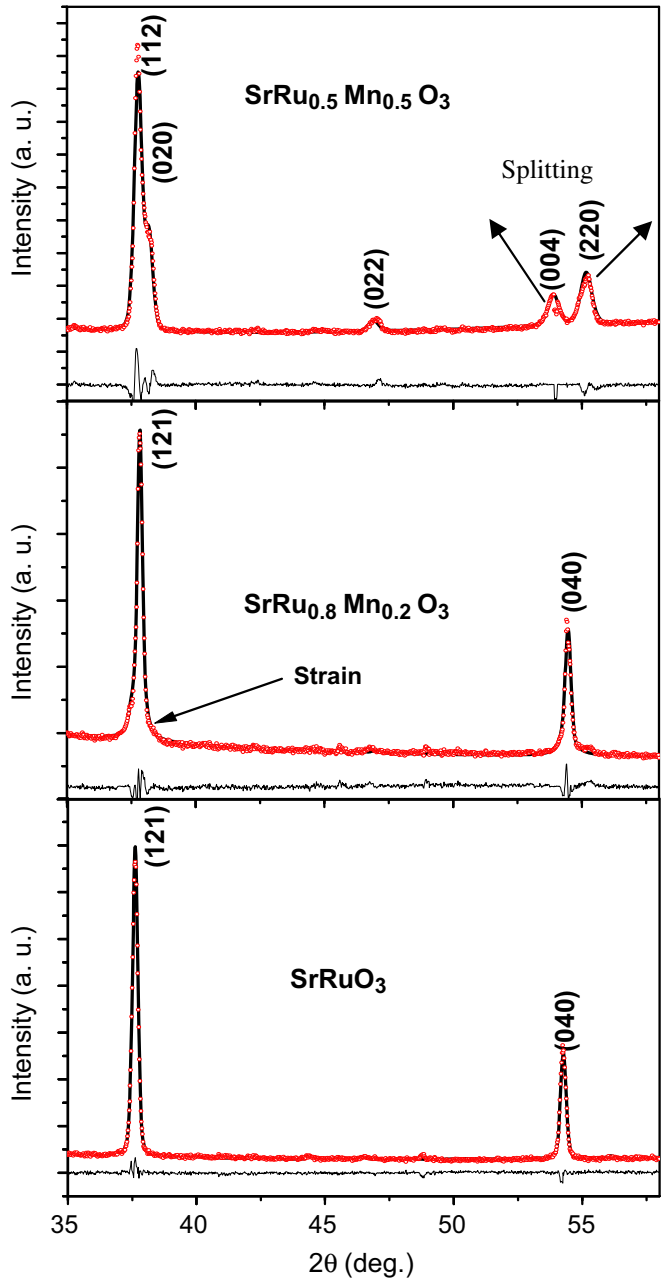

Fig. 2. Observed (symbol) and calculated (solid line) X-ray powder diffraction pattern for $SrRu_{1-x}Mn_xO_3$ measured at room temperature.

symmetry of the parent $SrRuO_3$ retains as an orthorhombic crystal symmetry with space group *Pnma* up to the doping concentration $x \sim 0.2$. Above the critical doping concentration, there is a clear splitting of the 040 peak into 004 and 220 peaks. In addition, the Rietveld analysis show that the experimental peaks are matched with the calculated peaks considering tetragonal crystal symmetry with space group *I*4/*mcm*. This suggests that the system undergoes transformation from orthorhombic crystal symmetry to tetragonal crystal symmetry at $x > 0.2$. It can be noted from the XRD peaks that the base of the peaks of $SrRu_{0.8}Mn_{0.2}O_3$ is broadened compared to the $SrRuO_3$ peaks due to chemical doping, indicating lattice strain induces before the structural transition in the system. The structural transition is due to increasing of the tolerance factor, $t = (Sr-O)/\sqrt{2}(B-O)$ (B=Ru, Mn). The tolerance factor for the parent $SrRuO_3$ is 0.99 and it increases with Mn doping that can be explained based on the existence of redox ionic pair between Ru and Mn (Ru^{+4} (0.62 Å)+Mn^{+4} (0.545 Å)↔Ru^{+5} (0.565 Å)+Mn^{+3}(0.645 Å). At an equal distribution of Ru and Mn in the crystal lattice i.e. $SrRu_{0.5}Mn_{0.5}O_3$, the average ionic radius of these ions to be 0.596 Å by assuming the ratio among all the ions is same which is smaller than the radius of the Ru^{+4} ion (0.62 Å) in $SrRuO_3$. The tolerance factor (t) increases due to Mn doping, which favors to stabilize the crystal structure of the doped $SrRuO_3$ in tetragonal crystal structure. The obtained lattice parameters and crystal symmetries are also matched with the neutron data of the series reported by Kolesnik et al [10]. We first make the correlation between transport and structural data up to the critical concentration, $x \sim 0.2$, where the crystal symmetry remains orthorhombic. The obtained bond angle data from the Rietveld analysis shows that the *B*–O–*B* angle changes from lower angle side (for $SrRuO_3 \sim 162^\circ$) to higher angle side (180°) due to Mn doping. In general, the increase in the bond angle of the perovskite manganite systems effectively increases the atomic orbital overlapping of the transition elements that enhances electron delocalization, and hence the conductivity of the system increases [19]. In contrast, the conductivity decreases due to Mn doping though the bond angle increases up to the critical doping concentration ($x \sim 0.2$). This suggests that crystal structure does not play a major role on the metal–insulator transition of $SrRu_{1-x}Mn_xO_3$ below the critical doping level. At $x \geq 0.2$, the crystal structure may attribute to the conduction mechanism up to some extent as the structure changes from orthorhombic to tetragonal. This suggests that some other factors apart from the crystal structure dominate the conduction mechanism in the series.

Next we turn to discuss the disorder effect on the electronic properties as suggested by several authors that existed in strongly correlated Mott–Hubbard ferromagnetic metallic systems [20,21]. Since $SrRuO_3$ is strongly correlated metallic system, doping of other transition elements may induce disorder magnetically or structurally in the host material that would increase the Coulomb repulsion strength (U) and reduce bandwidth (W). The uprising of the resistivity with Mn doping is suggestive of a gap opening near the Fermi level, e.g., due to a critical value U/W for a Mott-like transition in the Hubbard model. To understand the conduction mechanism, we have analyzed the resistivity data by fitting the Mott's variable range hopping (VRH) model, $\rho = \rho_0 \exp(T_0/T)^{1/n}$, where ρ_0 is the pre-factor and T_0 represents the characteristic temperature [22]. However, it is found that the experimental data based on the VRH model do not give linear plot for $x = 0.2$ and the data fits with the polaron model, $\rho = \rho_0 T \exp(E_p/k_B T)$ shown in Fig. 3a. It is observed that there is two slopes in the measured temperature region, $4.2\,K < T < 100\,K$ and $100\,K < T < 300\,K$. This can be explained based on the thermally assisted polaron hopping model. The Ru 4*d* orbital splits into two subsets, t_{2g} (three fold degeneracy) and e_g (two fold degeneracy) in octahedral

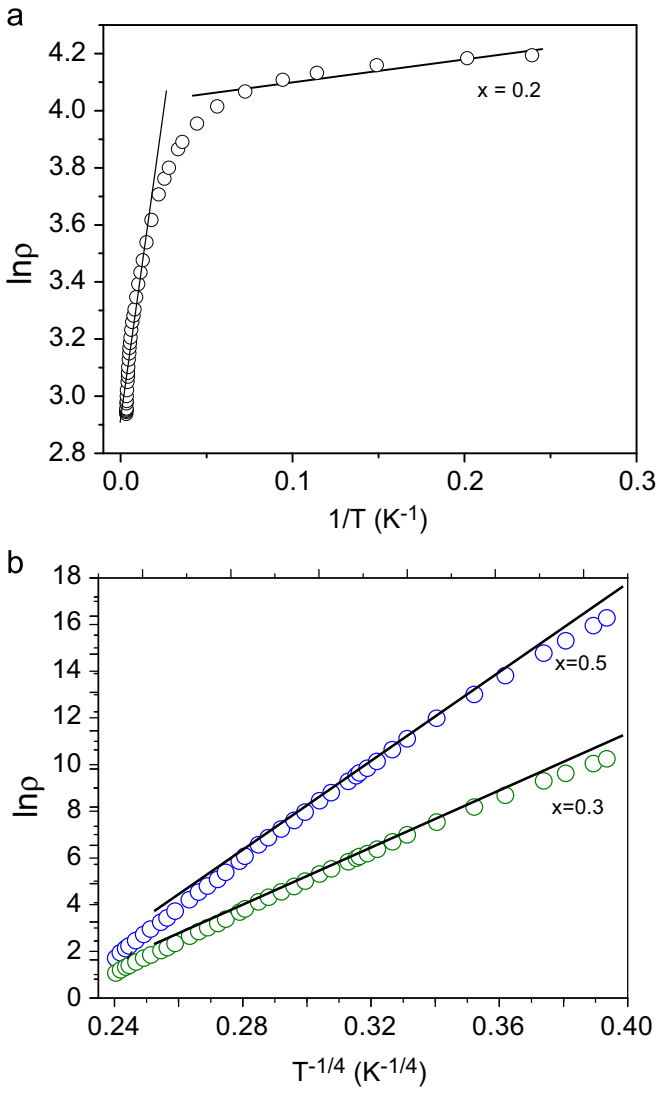

Fig. 3. (a) Polaron model fitted to the resistivity data for $x=0.2$ and (b) Mott's model fitted to the resistivity data for $x=0.3$ and 0.5.

environment. In general, the t_{2g} electrons are more localized than e_g electrons. Mn doping induces lattice distortion as observed from the XRD data (base of the $SrRu_{0.8}Mn_{0.2}O_3$ peaks broadened). Therefore, distortion of the octahedral cage of O atoms lowers the symmetry and further splits the e_g and t_{2g} levels. The electron is now more tightly bound, forming a so-called lattice polaron. The polaron behaves as a negatively charged particle with a larger mass and lower mobility than an isolated electron. Consequently, the conductivity is low at low temperature. At $T>100$ K, the thermal energy overcomes the trapping energy associated with the polaron that enhances the conductivity. On the other hand, the resistivity data for $x>0.2$ obeys the VRH model and gives linear dependence plot (Fig. 3b) when the power factor to be $n=4$ i.e. three-dimensional hopping. It can be noted that the VRH mechanism dominates the conduction in the temperature range $4.2\,K<T<200\,K$. The data show that the slope of the curve increases with increase of the Mn doping concentration, indicating the carrier hopping energy increases with the doping content. The increase of Mn content creates spin fluctuation and Columbic potential fluctuation. So, the charge carriers experience potential difference while moving from one site to another site. The localization of the charge carriers in a random potential can be calculated using VRH model in which the parameter T_0 is related to localization length ξ and magnetic potential U_m. Here, $\xi\,(=1/\alpha)$ can be calculated using the following equation, $kT_0=171\alpha^3U_m\nu$, where U_m is 2 eV and ν, the lattice volume per manganese ion is $5.7\times10^{-29}\,m^3$ [23]. It is found that the localization length decreases with increasing Mn concentration, 8.1 nm for $x=0.3$–3.1 nm for $x=0.5$. These values are physically plausible since the localization length exceeds the ionic radius of Ru and Mn. Correlation of transport properties with VRH model parameters suggests that the random magnetic potential due to weakening of the long range ferromagnetic ordering plays substantial role on the conduction properties of Mn doped $SrRuO_3$.

We have studied the valence band spectra and core spectra of Ru and Mn using XPS technique to understand the conduction mechanism spectroscopically. Before discussing the valence band spectra, we will address the very basic question of what is the valence of Ru and Mn in $SrRu_{1-x}Mn_xO_3$. This would be supportive to construct the possible charge carrier hopping mechanism in the framework of Zener's double exchange theory and would be useful to understand the effect of Mn on the conduction properties of $SrRuO_3$. Moreover, no detail study pertaining to valence states using XPS technique is available for this series. The parent compound is ionic with valence Sr^{+2}, Ru^{+4}, and O^{-2}, which would suggest that Mn would be in Mn^{+4} valence state upon doping for the charge neutralization. Also, it has been observed from several experimental techniques like neutron diffraction, Compton scattering measurement and mössbauer spectroscopy that the coexistence of trivalent 3*d* transition elements (M^{+3}) and Ru^{+5} seems to be a common phenomenon in the $CaRu_{1-x}M_xO_3$ system [24,25]. Therefore, it is plausible expectation that some part of the doped Mn has the +3 oxidation state rather than +4 and some part of Ru has the +5 oxidation state for the charge neutralization. As a result, it is expected that Ru and Mn may form mixed valence ionic states ($Ru^{+4}/Ru^{+5}\leftrightarrow Mn^{+3}/Mn^{+4}$). XPS binding energy is sensitive to the valence states of element as well as local environment. The concept of mixed valence states between Ru and Mn has been invoked while discussing the unusual role of Ru in manganite systems, $La_{1-x}A_xMnO_3$ [5–9]. The possible existence of mixed valence states will have different chemical bonding combinations such as Ru^{+4}–O–Mn^{+4}, Ru^{+4}–O–Mn^{+3}, Ru^{+4}–O–Ru^{+5}, Ru^{+4}–O–Ru^{+4}, Ru^{+5}–O–Ru^{+5}, Mn^{+4}–O–Mn^{+3}, Mn^{+3}–O–Mn^{+3}, Mn^{+4}–O–Mn^{+4}. Therefore, we can imagine that the possibility of multi peak structure under the broad envelope due to the chemical environment effect in XPS studies. Consequently, the analysis of peak binding energy and doublet peak energy separation would be an important ingredient to determine the valance state of Ru and Mn in this series and to understand the correlation effect. Fig. 4 shows the XPS Ru 3*d* and Ru 3*p* peak of $SrRu_{1-x}Mn_xO_3$. Previously reported XPS data of Ru based compounds show that the core 3*d* peak of Ru^{+5} appears at higher binding energy than Ru^{+4} and the difference is nearly 1.4 eV [26]. Moreover, the doublet peak energy separation ($\Delta E_{B.E}=B.E\ 3d_{5/2}-B.E\ 3d_{3/2}$) of Ru^{+5} is smaller than the Ru^{+4} ion since Ru^{+5} has weak spin–orbit coupling constant than $Ru^{+4}(\lambda=900\,cm^{-1})$. Since C 1*s* peak appears at the same position where the Ru $3d_{3/2}$ peak appears, therefore, all the peaks were normalized based on the Sr $3p_{3/2}$ peak (268.4 eV). Considering all these facts, we carry out the analysis of Ru 3*d* spectra in details and the peak positions were determined by fitting the theoretical profiles of the data. In the case of a compound containing Ru^{+4} ion, Ru $3d_{5/2}$ locates at 280.8 eV and Ru $3d_{3/2}$ peak locates at 284.9 eV. These energy positions are matched with the parent $SrRuO_3$ compound, therefore, we consider Ru exists only in Ru^{+4} state in $SrRuO_3$. However, a chemical shift is observed due to Mn doping. The doublet peaks of Ru 3*d* shift towards higher binding energy, could arise from the two factors namely; neighboring ion effect of Mn or valence effect. In the case of neighboring Mn ion, the peak is expected to

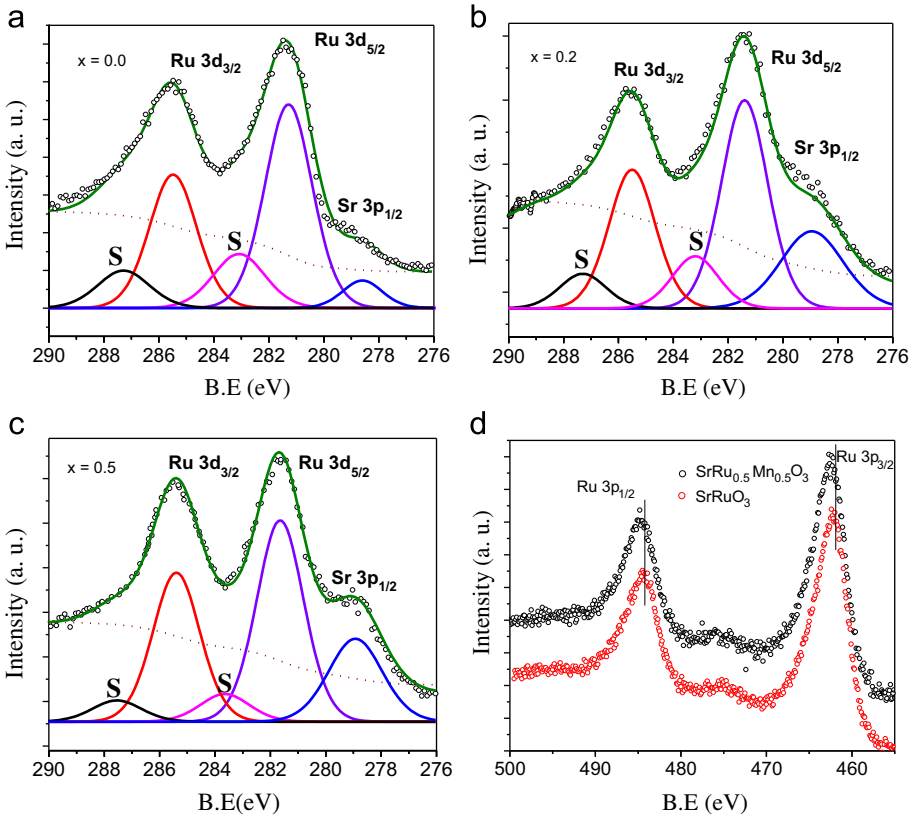

Fig. 4. Core Ru3*d* XPS spectra; the deconvolution of raw data consisting of main peak and satellite peak are shown in the figure (a) $x=0.0$, (b) $x=0.2$, and (c) $x=0.5$. Open circles show the experimental spectra, solid line passing through the experimental data is the summation of individual deconvoluted peak. The satellite deconvoluted peaks are denoted by S and rest is main peak of Ru 3*d* and Sr $2p_{1/2}$ shown in the figure. The deconvoluted peaks are plotted after the background subtraction. (d) Core Ru 3*p* spectra for $x=0.0$ and 0.5.

Table 1
Parameters obtained from deconvolution of XPS core Ru 3*d* spectra using CASA XPS software. The spectrum is normalized based on the Sr $3p_{3/2}$ peak binding energy. $\Delta E_{spin-orbit}$: spin–orbit splitting of the Ru 3*d* peak; Ru $\Delta E_{satellite}$: energy separation between the Ru main peak and the corresponding satellite peak; $I_{satellite}/I_{main}$: ratio of the intensities between the Ru 3*d* satellite and the main peak.

Compound name	Ru $3d_{5/2}$ *B.E.* (eV)	$\Delta E_{spin-orbit}$ (eV)	Ru $\Delta E_{satellite}$	$I_{satellite}/I_{main}$
$SrRuO_3$	280.8	4.1	2.2	0.35
$SrRu_{0.8}Mn_{0.2}O_3$	281.1	4.1	2.0	0.25
$SrRu_{0.5}Mn_{0.5}O_3$	281.4	3.85	2.1	0.15

shift towards lower binding energy since Ru is having more electronegativity value than Mn that would increase electron density at the Ru ion. Consequently, the binding energy of Ru 3*d* peak supposes to be decreased due to neighboring Mn ion effect. Moreover, the chemical shift occurs in the range of binding energy ± 0.2 eV when any electron donor or acceptor is directly attached to the Ru ion [27]. In contrast, we observe chemical shift towards higher binding energy and the shifting is significant, indicating the chemical shift is due to the change of valency rather than neighboring Mn ion effect. For 50% Mn doped $SrRuO_3$ sample the chemical shift of the main peak of Ru 3*d* is $\Delta E_{B.E}=0.6$ eV with respect to the $SrRuO_3$ sample (Table 1). The similar chemical shift without resolved peak between Ru^{+4} and Ru^{+5} was observed earlier in $CaRu_{1-x}Mn_xO_3$ [28]. The chemical shift indicates that Ru exits in Ru^{+4} and Ru^{+5} valence states. It is also observed from the Ru 3*d* spectrum that an asymmetric type of peak shape (called satellite peak) which appears at about 2.1 eV to the higher binding energy side of each of the Ru 3*d* doublet peaks. This indicates a significant deviation of the local environment of the emitting atom with respect to the bulk phase. Cox et al. [29] attributed the satellite peak to many body electrons and these effects can be understand based on the theory proposed by Kotani and Toyazawa [30]. To extract more information from the asymmetric shape of the main peak we carried out the spectral deconvolution mentioned in the experimental section. The calculated peaks are matched with the experimental data. The results of these spectral decompositions are shown in Fig. 4a, b, and c and the corresponding parameters are summarized in Table 1. It is to be noted that the minimum χ^2 value obtained for the $SrRu_{0.5}Mn_{0.5}O_3$ when the doublet peak energy separation was considered 3.85 eV in contrast to 4.1 eV for $SrRuO_3$, indicating suppression in the average spin–orbit coupling of $x=0.5$ sample. Besides, it is observed from the fitting data that the intensity ratio between the satellite peak to the main peak decreases with increasing Mn content. Earlier study of Ru based oxide system shows that the intensity of satellite peak for Ru^{+5} based oxides is lower than the Ru^{+4} based oxides [31]. This is due to the electron correlation effect since nearly 40% of electron reduces when the valence state of Ru changes from Ru^{+4} to Ru^{+5} [32]. To support the conclusion drawn about the valence states of Ru from the peak decomposition, we have also recorded Ru 3*p* core level spectrum (Fig. 4d). Both the Ru 3*p* peaks (Ru $3p_{3/2}$ and Ru $3p_{1/2}$) for $SrRu_{0.5}Mn_{0.5}O_3$ appear nearly 0.5 eV above than the peaks for $SrRuO_3$. The detail analysis of XPS core peak suggests that Ru exists as Ru^{+4} and Ru^{+5} ionic states in the Mn doped samples.

Next we analyze the Mn 2*p* and Mn 3*s* XPS peak for $SrRu_{0.5}Mn_{0.5}O_3$ (Fig. 5). To determine the valence states of Mn, we compare the binding energy and doublet peak energy separation of Mn 2*p* with the spectrum of reference sample,

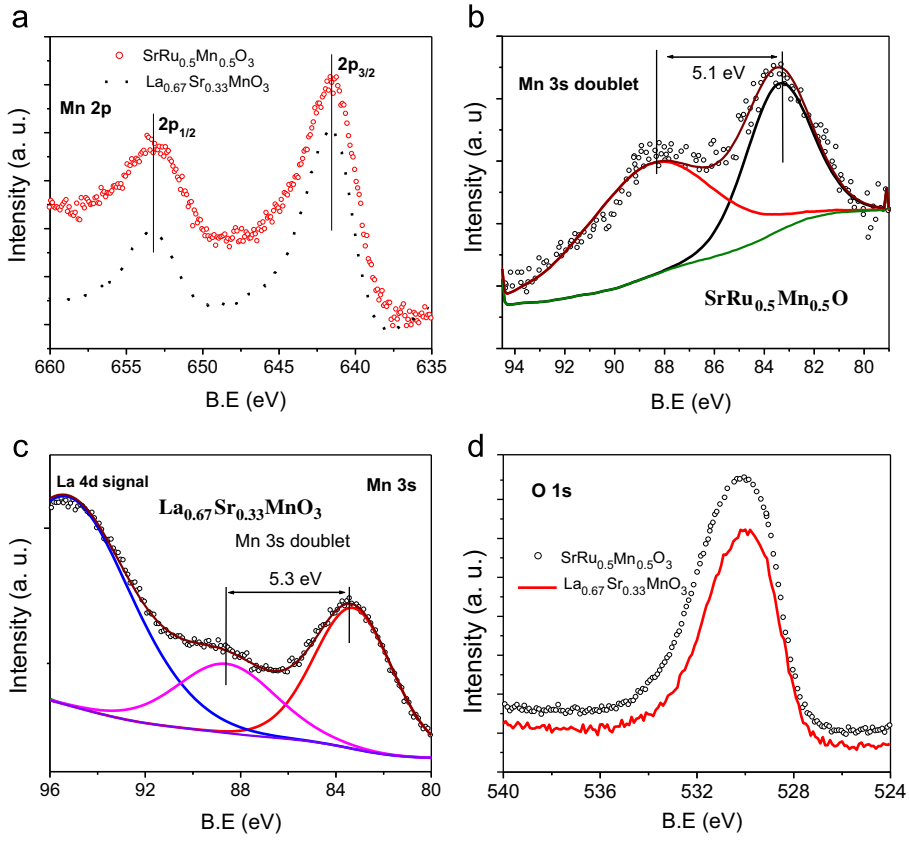

Fig. 5. Core Mn spectra for $SrRu_{1-x}Mn_xO_3$ ($x=0.5$) and compared with the data of $La_{0.67}Sr_{0.33}MnO_3$ to determine the valence states of Mn; (a) Mn2*p*, (b and c) Mn 3*s*, and (d) O 1*s*.

$La_{0.67}Sr_{0.33}MnO_3$, where Mn exists in mixed valence states (Mn^{+3} and Mn^{+4}) (Fig. 5a). Because of strong spin–orbit coupling, the Mn 2*p* peak splits into Mn $2p_{3/2}$ and Mn $2p_{1/2}$ with the doublet peak energy separation, $\Delta E_{s-o}=11.7$ eV. Moreover, a shake up peak at the position of ~5 eV higher energy side of the main peak appears in the spectra. The features such as position of 2*p* peak binding energy, doublet peak energy separation and shake up peak are well matched with the features of $La_{0.67}Sr_{0.33}MnO_3$, indicating Mn exists in mixed valence states (Mn^{+3}/Mn^{+4}). Besides, the value of the Mn 3*s* exchange splitting was used to determine the Mn valence in a more quantitative way than is possible by means of the Mn 2*p* signal (Fig. 5b and c). The doublet peak energy separation depends on the redistribution of the valence states of the Mn ions since the spin–orbit coupling constant is 180 and 138 cm^{-1} for Mn^{+3} and Mn^{+4} ion in octahedral environment, respectively. XPS study of manganite sample indicates that there is a linear relation between the Mn valence and the Mn 3*s* exchange splitting energy by the equation; $v_{Mn}=9.67-1.27\ \Delta E_{3s}$/eV [33]. The ΔE 3*s* value was estimated for both $SrRu_{0.5}Mn_{0.5}O_3$ and $La_{0.67}Sr_{0.33}MnO_3$ from the peak fitting procedure, in which the same constraint was imposed for both the samples. It is found from the peak fitting that the ΔE 3*s* is 5.1 eV for $SrRu_{0.5}Mn_{0.5}O_3$ and 5.3 eV for $La_{0.67}Sr_{0.33}MnO_3$. Further, the oxygen stoichiometry is nearly same in both the samples since the peak position and shape of the O 1*s* spectrum is identical (Fig. 5d). The calculated average valence state of Mn in $SrRu_{0.5}Mn_{0.5}O_3$ using the empirical equation is +3.5, indicating Mn exists both in Mn^{+4} and Mn^{+3} valence states. These XPS data suggest that Ru and Mn tend to form mixed ionic pair in the Mn doped $SrRuO_3$. However, the existence of mixed valence state of Mn enhances the delocalization of electron which ultimately shows good conductivity via double exchange process that observed in $La_{0.67}Sr_{0.33}MnO_3$ [16]. In contrast, $SrRu_{0.5}Mn_{0.5}O_3$ consisting of mixed Mn^{+4} and Mn^{+3} valence states exhibits insulating behavior. An increase in the resistivity of Mn doped $SrRuO_3$ in spite of the existence of the mixed ionic pair, suggesting some other factors are responsible for the metal–insulator transition in $SrRu_{1-x}Mn_xO_3$.

Valance band spectrum of $SrRuO_3$ is well studied using photoemission spectroscopy to understand the conduction mechanism of the sample. Based on the simulation studies, it has been concluded that the valence peak consists of screened peak caused by coherent band (the quasiparticle band near E_F) and unscreened peak related to the incoherent band (the remnant of the Hubbard band between 1 and 2 eV) of the valence band [11]. The intensity ratio between the screened peak and unscreened peak has become a tool to distinguish between metallic and insulating ruthenates. In the case of metallic ruthenates, the screened peak becomes more pronounced over the unscreened peak and it is reversed in the case of insulating ruthenates. Therefore, study on the valence band spectra using photoelectron spectroscopy would be useful further to explain the doping induced metal–insulator transition. Fig. 6 shows the valence band spectra obtained using Al $K\alpha$ source. The spectrum of $SrRuO_3$ measured at $T=300$ K exhibits an intense coherent peak around ~0.8 eV, consistent with the earlier report [13]. The spectral analysis as per the observed features of the earlier reported data for $SrRuO_3$ suggests that the feature below ~3 eV is predominantly contributed by Ru t_{2g} and the peak at ~6 eV mainly arises from the O 2*p*. The closer view of the data below 4 eV after the subtraction of O 2*p* character indicates that the intensity of coherent peak decreases significantly with Mn doping (Fig. 6b) and the peak position coincides with the unscreened peak that observed earlier in insulating ruthenates [11]. These results are

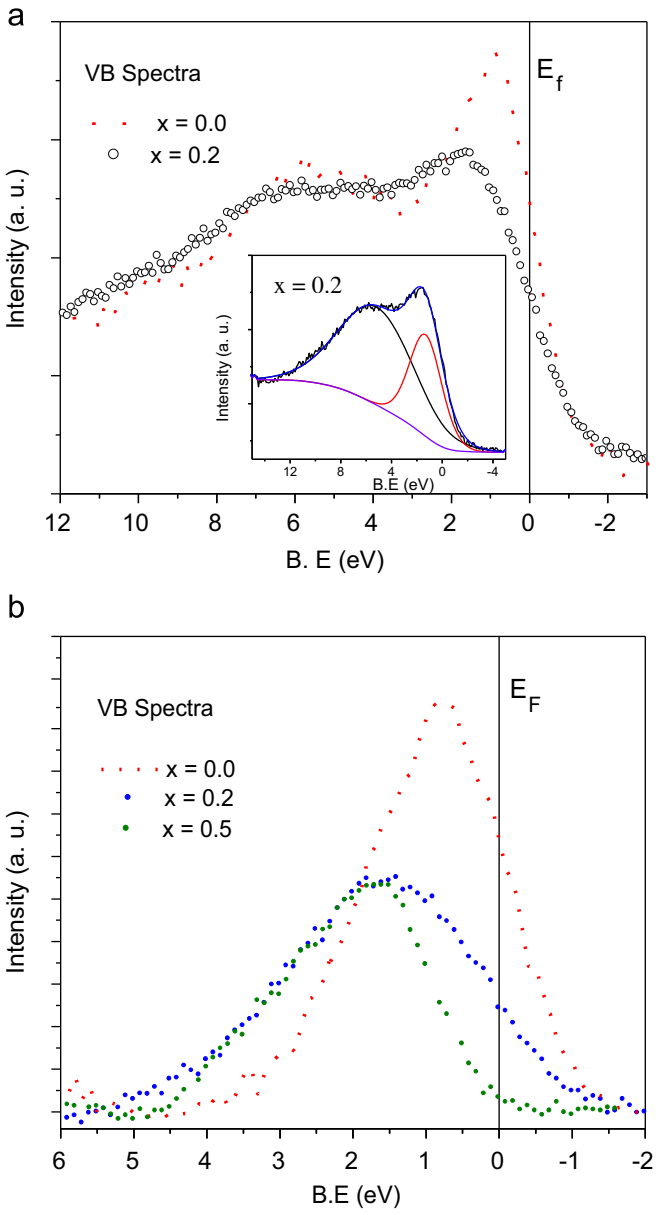

Fig. 6. (a) Valence band spectra of $SrRu_{1-x}Mn_xO_3$ measured using XPS technique at room temperature. The inset showing the deconvolution procedure of valence band spectrum for $x=0.2$ in order to know the amount of O 2*p* contribution. The same deconvolution procedure was followed for other samples. (b) Valence band spectra of $SrRu_{1-x}Mn_xO_3$ after the subtraction of the O 2*p* contributions.

consistent with the results reported recently by Horiba et al. [34]. This implies that doping of Mn drives the system from metallic to insulating state. Therefore, it can be concluded that electron correlation effect plays a major role on the doping induced metal to insulator transition in $SrRu_{1-x}Mn_xO_3$ [12].

In order to understand the electron correlation factors dominate the metal–insulator transition, we have calculated density of states (DOS). Total DOS (TDOS) for $SrRuO_3$ obtained from LSDA and LSDA+*U* calculations are shown in Fig. 7a. On comparing the TDOS corresponding to LSDA calculation with the valence band spectrum shown in Fig. 6a one can easily make out that LSDA result is not the true representation of the experimental data. The experimental data show a peak around 0.8 eV whereas TDOS show a peak around the Fermi level. Moreover, the magnetic moment obtained from LSDA calculation is $\sim 0.8\,\mu_B$/fu, which is significantly less than the experimental value of $\sim 1.7\,\mu_B$/fu [35].

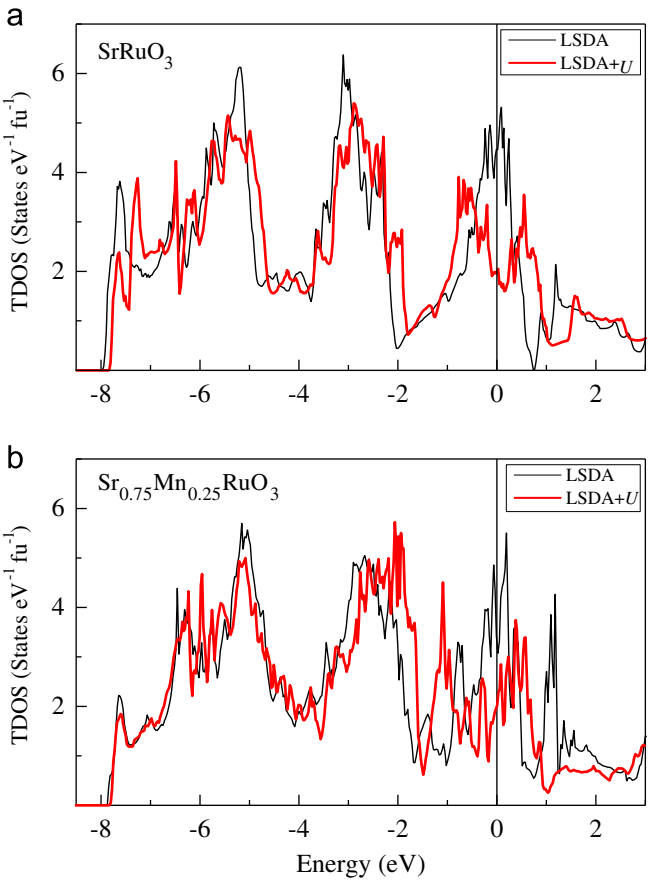

Fig. 7. Total density of states of (a) $SrRuO_3$ and (b) $SrRu_{0.75}Mn_{0.25}O_3$ obtained from LSDA and LSDA+*U* calculations.

These results clearly show the inadequacy of LSDA in expressing the electronic and magnetic properties of $SrRuO_3$, and suggest the importance of on-site Coulomb correlation in deciding these electronic properties. On considering $U=2$ eV for the Ru 4*d* electrons in the calculation, the value of magnetic moments is found to be $\sim 2\,\mu_B$/fu and the TDOS obtained from LSDA+*U* calculation provide a good representation of the experimental valence band spectrum with a peak around 0.7 eV. The small discrepancy in the peak position of the experimental spectrum and calculated TDOS may be attributed to the surface contribution to the experimental data as reported by Maiti and Singh [36]. It is important to note that the on-site Coulomb interaction strength of about 2 eV provides a good representation of the electronic and magnetic properties of other 4*d* electron system [37].

As mentioned earlier that the doping of Mn at the Ru sites reduces the intensity of the coherent peak and it moves to the higher binding energy, Fig. 7b. In order to understand the doping effect we have calculated the TDOS of one of the Mn doped samples having composition $Sr_{0.75}Mn_{0.25}RuO_3$ to describe the role of Coulomb interaction. The TDOS data by LSDA calculation does not show the correct representation of the experimental data. Therefore, we extend the calculation by imposing Coulomb interaction in the equation. The TDOS obtained from LSDA+*U* ($U^{3d}_{Mn}=5$ eV and $U^{4d}_{Ru}=2$ eV) are shown in Fig. 7b. It is important to note that the 3*d* electrons are more localized than the 4*d* electrons, therefore the values of on-site Coulomb interaction of Mn 3*d* electrons is expected to be more than that of the Ru 4*d* electrons. On comparing the TDOS of $Sr_{0.75}Mn_{0.25}RuO_3$ compound with that of $SrRuO_3$ one can easily find the decrement in the intensity of the coherent peak along with its shift to the higher

binding energy of 1.1 eV. Thus, our LSDA+U results give the qualitative understanding of doping induced metal–insulator transition observed in this series of compound and the electron localization caused by Coulomb correlation appears to be the driving mechanism for the metal–insulator transition.

The metal–insulator transition at $x \geq 0.2$ is confirmed from the electrical transport and spectroscopic results. We first describe the origin of metallic properties of the parent $SrRuO_3$ compound. $SrRuO_3$ crystallizes in an orthorhombic structure with 4 formula units per cell. In the ionic model, the four d electrons of Ru^{+4} occupy the triplet t_{2g} (d_{xy}, d_{yz}, d_{zx}) and leave the higher e_g doublet ($d_x{}^2{}_{-y}{}^2$, d_z^2) empty under the octahedral crystal field. The total bandwidth is about 3.1 eV due to the splitting of the t_{2g} band in distorted octahedral environment. However, the extent of distortion is not very strong in $SrRuO_3$. As a consequence, the system shows metallic behavior and it lies near the boundary of Mott–Hubbard system. Since 3d orbitals are less extended compared to 4d orbitals, Mn doping in $SrRuO_3$ induces strong Coulomb interaction (U). Consequently, the electron correlation effect increases with increasing Mn doping that reduces the spectral weight near the Fermi energy level as observed from valence band spectra and DOS calculation wherein the intensity of screened peak decreases and intensity of unscreened peak intensity increases with doped ions. The electron correlation effect ultimately opens a gap near the Fermi level. Further, XPS data show the presence of mixed valence states of Ru and Mn in doped $SrRuO_3$, $Ru^{+4}/Ru^{+5} \leftrightarrow Mn^{+4}/Mn^{+3}$. However, the charge carrier hopping between Ru^{+4} ($t_{2g}^3\uparrow t_{2g}^1\downarrow e_g^0$) and Mn^{+4} ($t_{2g}^3\uparrow e_g^0$) or Ru^{+4} ($t_{2g}^3\uparrow t_{2g}^1\downarrow e_g^0$) and Mn^{+3} ($t_{2g}^3\uparrow e_g^1$) is energetically unfavorable since spins down electrons of Ru need to be spin flip along the spin up direction during the exchange process as per the rule of spin conservation [38]. The possible energetically favorable charge carrier hopping sites are Mn^{+3} ($t_{2g}^3\uparrow e_g^1$) and Ru^{+5} ($t_{2g}^3\uparrow e_g^1$), and Mn^{+3} ($t_{2g}^3\uparrow e_g^1$) and Mn^{+4} ($t_{2g}^3\uparrow e_g^0$) because of spin symmetry. The presence of non-hopping sites disrupts the network of delocalization path for the charge carriers by which the charge carriers get localized, which reduces the number of hopping sites (Z). Besides, Mn doping induces spin fluctuation, which creates random potential that further reduces mobility of the charge carrier (t). As a result, Mn doping reduces one electron bandwidth (W) of $SrRuO_3$ since $W \sim 2Zt$ where Z is the number of hopping sites and t is the transfer integral. Therefore, the Coulomb correlation effect in conjugation with localization of the charge carriers caused by decrease the number of hopping sites reduces the spectral weight near the Fermi level. Such a progressive reduction in W with increasing Coulomb repulsion strength leads to the value of U/W to cross the critical value for the metal–insulator transition that creates soft band gap for $x=0.2$ and hard band gap for $x=0.5$. Hitherto, the resistivity increases several folds by Mn doping and $SrRuO_3$ exhibits insulating behavior at the critical doping level, $x \geq 0.2$.

In summary we have investigated the effect of Mn doping on valency and electronic properties of $SrRuO_3$ to understand the mechanism associated with the metal–insulator transition in the series. Valence band spectra in conjugation with the electrical measurement indicate that the parent $SrRuO_3$ undergoes metal to insulator transition at the critical Mn doping concentration $x \sim 0.2$. The X-ray photoelectron spectroscopy data show that Ru and Mn exhibit mixed valency state, $Ru^{+4}/Ru^{+5} \leftrightarrow Mn^{+3}/Mn^{+4}$. Though mixed valence ionic pair is the key ingredient for enhancement of the conductivity based on the framework of Zener's double exchange theory, the results reveal that Mn doping does not favor the double exchange interaction in $SrRuO_3$. The detail analysis of the data implies that Mn doping increases the Coulomb repulsion interaction and reduces the number of hopping sites in $SrRuO_3$. Consequently, the doping of Mn decreases the spectral weight near the Fermi energy level thereby the system undergoes metal–insulator transition at $x \geq 0.2$. This study helps to understand the metal–insulator transition in $SrRu_{1-x}Mn_xO_3$ and can be extended to support for understanding the conductivity mechanism in the case of doping of other 3d transition elements in $SrRuO_3$.

References

[1] S.C. Gausepohl, M. Lee, L. Antognazza, K. Char, Appl. Phys. Lett. 67 (1995) 1313.
[2] K.S. Takahashi, A. Sawa, Y. Ishii, H. Akoh, M. Kawasaki, Y. Tokura, Phys. Rev. B 67 (2003) 094413.
[3] K. Maiti, Phys. Rev. B 77 (2008) 212407.
[4] D. Kasinathan, D.J. Singh, Phys. Rev. B 74 (2006) 195106.
[5] P.V. Vanitha, A. Arulraj, A.R. Raju, C.N.R. Rao, C.R. Acad. Sci. Ser. IIc: Chim. 2 (1999) 595.
[6] R.K. Sahu, Z. Hu, M.L. Rao, S.S. Manoharan, T. Schmidt, B. Richter, M. Knupfer, M. Golden, J. Fink, C.M. Schneider, Phys. Rev. B 66 (2002) 144415.
[7] R.K. Sahu, M. Qureshi, M. L Rao, S.S. Manoharan, A.K. Nigam, Appl. Phys. Lett. 80 (2002) 88.
[8] R.K. Sahu, P.S.R. Krishna, A. Das, A.B. Shinde, M. Ramanadham, J. Magn. Magn. Mater. 297 (2006) 84.
[9] C. Martin, A. Maignan, M. Hervieu, C. Autret, B. Raveau, D.I. Khomskii, Phys. Rev. B 63 (2001) 174402.
[10] S. Kolesnik, B. Dabrowski, O. Chmaissem, Phys. Rev. B 78 (2008) 214425.
[11] K. Fujioka, J. Okamoto, T. Mizokawa, A. Fujimori, I. Hase, M. Abbate, H.J. Lin, C.T. Chen, Y. Takeda, M. Takano, Phys. Rev. B 56 (1997) 6380.
[12] H.-D. Kim, H.-J. Noh, K.H. Kim, S.-J. Oh, Phys. Rev. Lett. 93 (2004) 126404.
[13] J.M. Rondinelli, N.M. Caffrey, S. Sanvito, N.A. Spaldin, Phys. Rev. B 78 (2008) 155107.
[14] S.H. Vosko, L. Wilk, M. Nusair, Can. J. Phys. 58 (1980) 1200.
[15] L. Klein, J.S. Dodge, C.H. Ahn, G.J. Snyder, T.H. Geballe, M.R. Beasley, A. Kapitulnik, Phys. Rev. Lett. 77 (1996) 2774.
[16] C. Zener, Phys. Rev. 81 (1951) 440.
[17] T. Okuda, Y. Tomioka, A. Asamitsu, Y. Tokura, Phys. Rev. B 61 (2000) 8009.
[18] R. Gross, L. Alff, B. Büchner, B.H. Freitag, C. Höfener, J. Klein, Y. Lu, W. Mader, J.B. Philipp, M.S.R. Rao, P. Reutler, S. Ritter, S. Thienhaus, S. Uhlenbruck, B. Wiedenhorst, J. Magn. Magn. Mater. 211 (2000) 150.
[19] G. Srinivasan, D. Hanna, Appl. Phys. Lett. 79 (2001) 641.
[20] K.W. Kim, J.S. Lee, T.W. Noh, S.R. Lee, K. Char, Phys. Rev. B 71 (2005) 125104.
[21] K. Yamaura, D.P. Young, E. Takayama-Muromachi, Phys. Rev. B 69 (2004) 024410.
[22] A.L. Efros, M. Pollak (Eds.), Electron–Electron Interactions in Disordered Systems, Elsevier, Amsterdam, , 1986.
[23] A.J. Millis, Nature 392 (1998) 147.
[24] T. Taniguchi, S. Mizusaki, N. Okada, Y. Nagata, K. Mori, T. Wuernisha, T. Kamiyama, N. Hiraoka, M. Itou, Y. Sakurai, T.C. Ozawa, Y. Noro, H. Samata, Phys. Rev. B 75 (2007) 024414.
[25] A. Koriyama, M. Ishizaki, T. Taniguchi, Y. Nagata, T. Uchida, H. Samata, J. Alloys Compd. 372 (2004) 58.
[26] D. Briggs, in: D. Briggs, M. P Seah (Eds.), Practical Surface Analysis, 2nd edn, vol. 1, John Wiley, Chichester, 1992, p. 437.
[27] K. Kobayashi, H. Ohtsu, T. Wada, T. Kato, K. Tanaka, J. Am. Chem. Soc. 125 (2003) 6729.
[28] T. Taniguchi, S. Mizusaki, N. Okada, Y. Nagata, S.H. Lai, M.D. Lan, N. Hiraoka, M. Itou, Y. Sakurai, T.C. Ozawa, Y. Noro, H. Samata, Phys. Rev. B 77 (2008) 014406.
[29] P.A. Cox, R.G. Egdell, J.B. Goodenough, A. Hamnett, C.C. Naish, J. Phys. C 16 (1974) 912.
[30] A. Kotani, Y. Toyazawa, J. Phys. Soc. Jpn. 37 (1974) 912.
[31] U. Manju, V.P.S. Awana, H. Kishan, D.D. Sarma, Phys. Rev. B 74 (2006) 245106.
[32] Z. Hu, H. von Lips, M.S. Golden, J. Fink, G. Kaindl, F.M.F. de Groot, S. Ebbinghaus, A. Reller, Phys. Rev. B 61 (2000) 5262.
[33] E. Beyreuther, S. Grafström, L.M. Eng, C. Thiele, K. Dörr, Phys. Rev. B 73 (2006) 155425.
[34] K. Horiba, H. Kawanaka, Y. Aiura, T. Saitoh, C. Satoh, Y. Kikuchi, M. Yokoyama, Y. Nishihara, R. Eguchi, Y. Senba, H. Ohashi, Y. Kitajima, S. Shin, Phys. Rev. B 81 (2010) 245127.
[35] G. Cao, S. McCall, M. Shepard, J.E. Crow, R.P. Guertin, Phys. Rev. B 56 (1997) 321.
[36] K. Maiti, R.S. Singh, Phys. Rev. B 71 (2005) 161102(R).
[37] S.K. Pandey, K. Maiti, Phys. Rev. B 78 (2008) 045120.
[38] E.O. Wollan, W.C. Koehler, Phys. Rev. 100 (1955) 545.